Pattern Recognition in Time Series for Space Missions: A Rosetta Magnetic Field Case Study

K. Ostaszewski[a,*], P. Heinisch[a], I. Richter[a], H. Kroll[b], W.-T. Balke[b], D. Fraga[c], K.-H. Glassmeier[a]

[a]*Institut für Geophysik und extraterrestrische Physik, Technische Universität Braunschweig, Germany*
[b]*Institut für Informationssysteme, Technische Universität Braunschweig, Germany*
[c]*ESA/ESAC, ES-28691, Urb. Villafranca del Castillo, Madrid, Spain*

Abstract

Time series analysis is a technique widely employed in space science. In unpredictable environments like space, scientific analysis relies on large data sets to enable interpretation of observations. Artificial signal interferences caused by the spacecraft itself further impede this process. The most time consuming part of these studies is the efficient identification of recurrent pattern in observations, both of artificial and natural origin, often forcing researchers to limit their analysis to a reduced set of observations. While pattern recognition techniques for time series are well known, their application is discussed and evaluated primarily on purpose built or heavily preprocessed data sets. The aim of this paper is to evaluate the performance of state of the art pattern recognition techniques in terms of computational efficiency and validity on a real-life testcase. For this purpose the most suitable techniques for different types of pattern are discussed and subsequently evaluated on various hardware in comparison to manual identification. Using magnetic field observations of the ESA Rosetta mission as a representative example, both disturbances and natural patterns are identified. Compared to manual selection a speed-up of a factor up to 100 is achieved, with values for recall and precision above 80%. Moreover, the detection process is fully automated and reproducible. Using the presented method it was possible to detect and correct artificial interference. Finally, the feasibility of onboard deployment is briefly discussed.

Keywords: Rosetta, Time Series, Machine Learning, Magnetic Field, Pattern Recognition

1. Introduction

In recent years machine learning algorithms have shown prominence in the context of time series analysis. While the range of possible application is never-ending, the common benefit is the performance of a task in a quick and automated fashion. The latter characteristics render the application of machine learning interesting for space science and technology.

*Corresponding author
Email address: k.ostaszewski@tu-bs.de (K. Ostaszewski)

In the past their applicability has been, amongst other use cases, investigated in the context of star classification [1–3], spacecraft health monitoring [4, 5], space weather analysis [6] and magnetometer data processing [7]. However, previous work focused mainly on analysis of scientific data (time series forcasting, classification, object detection in images) or leveraged a specific sensor configuration. In this paper we showcase the applicability of machine learning algorithms for pattern recognition to enable large scale statistical studies. In unpredictable environments like space, scientific analysis relies on large data sets to enable interpretation of observations. The most time consuming part of these studies is the efficient identification of recurrent pattern in observations. The overhead of manual selection often forces scientists to limit their analysis to a reduced set of observations. A good example is the vast amount of data returned by the ESA Rosetta mission [8–10]. The Rosetta mission was the first of its kind that allowed scientists to study the interaction of the solar wind with the comet 67P/Churyumov-Gerasimenko (67P/CG) over the course of its journey around the sun. The comparatively long mission duration of more than two years resulted in an extraordinary large dataset. Manual analysis of data is, therefore, a very time consuming and tedious task and sometimes nearly impossible, making it a suitable example to demonstrate the benefits of machine learning. By employing machine learning algorithms the identification process of patterns can be significantly accelerated compared to manual selection, which in turn enables the use of a larger dataset for statistical analysis. The advantages of pattern recognition do not only apply to offline scientific analysis. Moreover, it can be applied for real-time data analysis to identify interesting patterns and to correspondingly adapt trajectories or dynamically allocate downlink bandwidth. This is especially important for future mission like JUICE [11] and BepiColombo [12] whose aim it is to investigate structures in great detail in the magnetosphere and atmosphere of Jovian moons and planet Mercury respectively. The datasaets used in this study are made available through the ESA Planetary Science Archive [13] and the Planetary Data System of NASA.

The focus will be put on patterns in the magnetic field, the concepts are, however, extendable to any other kind of time series. Scientists were able to observe specific recurrent patterns in the magnetic field and other plasma quantities [14–17]. Because of their complexity these patterns can in general not be identified by simple statistical or spectral measures. Additionally, disturbances caused by the spacecraft, sensor noise and changing background conditions further impede the identification process. Both, the identification of artificial and natural patterns requires specifically trained scientists. Even then, manual selection has the drawbacks of not being reproducible and being prone to visual bias. In order to solve this problem we demonstrate on a real-world test case how patterns, both artificial and natural, can be recognized in an efficient, automated and reproducible fashion using machine learning algorithms. This study is organized as follows. Firstly, a representative example for natural and artificial patterns respectively is presented. Subsequently, suitable detection methods depending on the nature of the pattern and data processing are discussed. In Section 3 details on implementation for the latter methods are given, followed by their evaluation in terms of statistical validity and computational complexity in Section 4.

2. Time Series Analysis for Space Missions

In this context statistical analysis of time series is a powerful tool [18, 19]. However, to enable scientific interpretation artificial interferences have to be identified and, if possible, corrected beforehand [7]. Contrary to controlled laboratory measurements, instruments on board of spacecrafts are subject to unavoidable interferences. Typical sources include attitude changes, thrusters, heaters, solar panels and other spacecraft systems [16, 20, 21]. Distinguishing between artificial disturbances and natural variations is challenging [20]. Even though ground based reference models are standard for many missions, testing of complex systems (e.g. propulsion) is unfeasible in many cases. Therefore, interferences have to be identified and corrected during or after flight.

In the study of celestial objects many kinds of time series can be encountered. Typical examples are seismic activity [22, 23], plasma interaction [24–28], astronomical spectroscopy [29] and exoplanet detection [30–32]. Because of the complexity of observations pattern detection is, in most cases, performed manually [15, 17, 33].

In the following magnetic field data obtained during the Rosetta mission is used as an representative example to showcase the benefits, problems and limitations of automated pattern recognition for time series. Because of high demands for active trajectory control and the novelty of scientific observations, combined with a comparatively long mission duration, the Rosetta mission offers a divers data set. Magnetic field measurements were chosen because they have three components and are very sensitive to different kinds of interferences. Therefore, they can be considered as a worst case scenario. Onboard the Rosetta spacecraft two fluxgate magnetometers with a measurement range of $\pm$16384 nT, resolution of 31 pT and noise level of 22 pT/ $\sqrt{\text{Hz}}$ were employed [34]. The measurements were calibrated following Richter et al. [16] and Goetz et al. [15] to remove offset errors, temperature drifts and spacecraft influences. For a detailed description of the data quality see [35–41]. However, as the focus of this study lies solely on the detection of patterns, without any scientific interpretation of these structures, the data quality is of secondary importance.

2.1. Patterns in the Magnetic Field

The top panel of Figure 1 shows an example of an artificial disturbance in the magnetic field. In the shaded area short, recurring drops in the magnetic field are visible. These disturbances are caused by Orbit Correction Maneuvers using thrusters, which occurred frequently to change Rosettas trajectory. In the bottom panel the current associated with thruster heaters is displayed. As the heaters are active during thruster firerings, the current directly correlates with the occurrences of Orbit Correction Maneuvers, however it is not the inducing source of the disturbances. Nevertheless, the pattern in the heater current can be used as an additional criterion for identification and to define regions of interest. A direct source is often not identifiable, as processes on board the spacecraft include multiple systems activated simultaneously or in very short succession. As the source of these disturbances is based, in most cases, on a strictly defined routine, they have the distinct characteristic of being reproducible in length and shape.

As an example for pattern of scientific interest, large asymmetric magnetic field enhancements, in the following referred to as Steepened Waves, are chosen. Multiple occurrences of these Steepened Waves are shown in Figure 2.

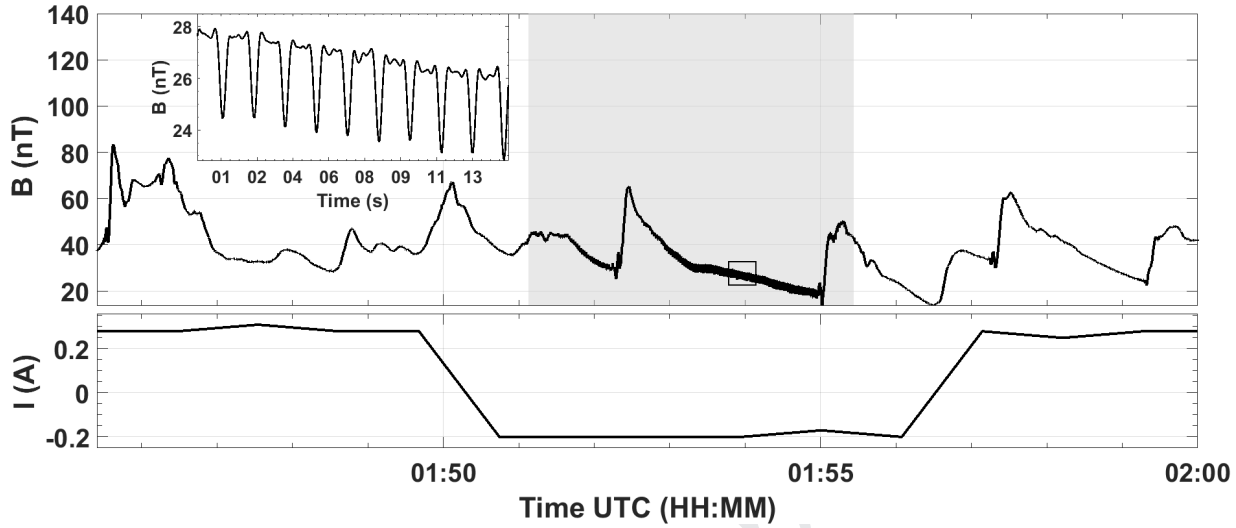

Figure 1: The top panel shows an example of the influence of Orbit Correction Maneuvers on the magnetic field on August, 1st 2015. The current for the thruster heaters (NPWDA320) is shown in the bottom panel. The shaded area marks the time interval in which interferences are visible in the magnetic field.

They are characterised by a sudden sharp increase in magnetic field, directly followed by a slowly decreasing edge. In general structures of scientific interest are governed by highly dynamical background conditions and have, therefore, a highly variable shape. This circumstance significantly complicates automated detection.

2.2. Methods

Depending on the properties of the time series and the pattern, different approaches to pattern recognition are possible. One possibility is to use a similarity measure based on a metric to find patterns similar in shape to a reference pattern. Popular measures are for example cross-correlation, Constraint Dynamic Time Warping [42] and euclidean distance. However, this approach only works well for exact replicas of the reference pattern, which makes them perfectly suited for the detection of interferences. While Constrained Dynamic Time Warping is a widely used and popular method [43, 44], it is susceptible to scaling and offsets. Hence, additional computationally expensive preprocessing steps are needed. The same argument applies to euclidean distance with the addition that it is not invariant to temporal shift. In contrast cross-correlation is invariant to scaling, temporal shift and offsets. In comparison to Constrained Dynamic Time Warping and euclidean distance it performed best in terms of computational efficiency and statistical validity for this use case.

Other possible pattern recognition techniques are Hidden Markov Models [45] or deep learning methods, e.g Long Short Term Memory (LSTM) networks [46] and 1D Convolutional Neural Networks [47]. Compared to the shape based similarity approach the latter methods have the advantage that they can identify patterns by their characteristics instead of similarity to a reference pattern. Patterns induced by physical processes are subject to strong

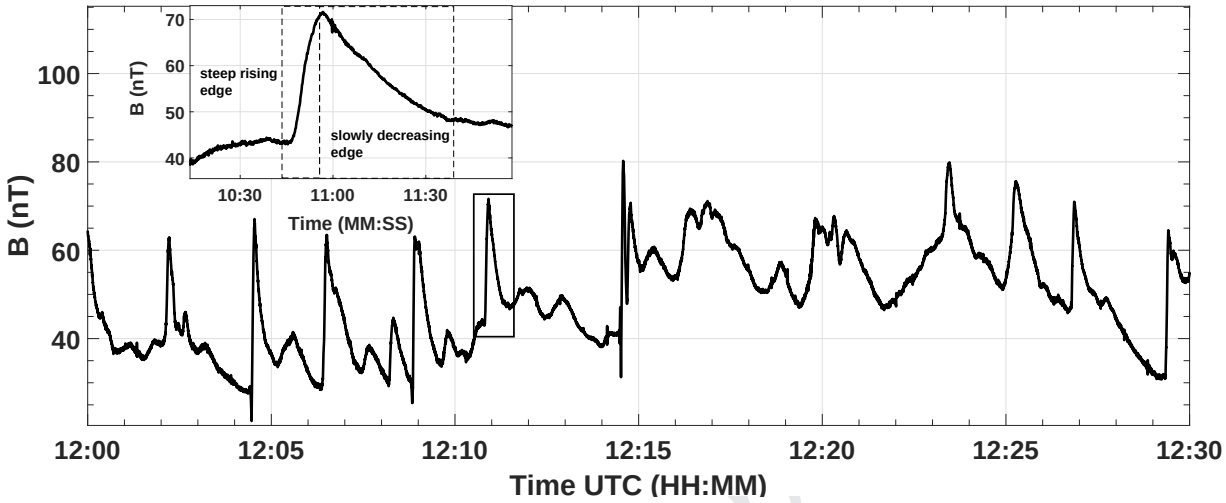

Figure 2: The magnetic field is shown for an exemplary time interval of 30 min on July, 27th 2015. Multiple occurrences of Steepened Waves with different amplitude and width are visible.

variations because of highly variable general conditions and general instability of the process. For these kind of patterns Hidden Markov Models and deep learning methods are better suited then similarity measures. Hence, LSTM networks are used for pattern recognition in the case of Steepened Waves, whereas for Orbit Correction Maneuvers cross-correlations is employed.

2.3. Data Preprocessing

Preprocessing of data is an integral step in pattern recognition as the quality of the data directly affect the success rate of recognition, especially for deep learning methods. The patterns discussed in the previous section have varying amplitudes and occur at different time scales. For the absolute amplitude a lower threshold is used to filter the observations. As only the relative amplitude is of importance for pattern recognition, the magnetic field B is normalized as follows:

$$\mathrm{B}_n = \frac{\mathrm{B} - \min(\mathrm{B})}{\max(\mathrm{B}) - \min(\mathrm{B})}. \tag{1}$$

Moreover, having features with widely different scales may cause the network to weight them differently, which in turn can lead to bad convergence. In some cases it can even prevent the network from learning successfully. In order to improve convergence normalization of input data is a necessity. To handle different time scales the data is downsampled to different sampling frequencies $f_1 = f_0/f_{rs}$, where $f_0 = 20\,\mathrm{Hz}$ is the magnetometer sampling frequency and f_{rs} is a resampling factor. Pattern recognition is then performed for every downsampled data set independently. Additionally, a 6th order butterworth [48] low-pass filter with a cut-off frequency of 200 mHz was

applied to remove high frequency sensor noise. For the cross-correlation based approach no preprocessing steps are needed.

3. Implementation

3.1. Cross-correlation

In the following section, implementation details on how to efficiently identify and correct Orbit Correction Maneuvers with cross-correlation are discussed. The cross-correlation of two discrete time series f and g is defined as

$$(f \star g)(\tau) = \sum_{t=-\infty}^{\infty} f(t)^* g(t+\tau), \tag{2}$$

where $f(t)^*$ denotes the complex conjugate of $f(t)$. In practice, cross-correlation is implemented using Fast Fourier Transform to reduce run time complexity from $O(N^2)$ to $N \log(N)$ [49, 50]. However, as the frequency resolution scales with the window length this implementation is not suited for the small window sizes (2 s) in the case of Orbit Correction Maneuvers. Hence, an implementation based on Equation (2) is used. For the initial search one example of a pattern for the current and magnetic field respectively, as seen in Figure 1, is used as a reference signal. An Orbit Correction Maneuver is successfully identified if both the pattern in the magnetic field as well as the pattern in the current are matched. For detection a sliding window approach is employed. However, as a single example of the disturbance can be overlapped by other disturbances and natural variations, its shape is not representative. To improve results all interferences identified in the first pass are classified by the shape based clustering algorithm k-Shape [49]. The algorithm sorts signals into clusters based on their distance to an average cluster shape S, which is obtained by computing the average of the aligned signals in the cluster. Each S is then used as a new reference signal to identify more disturbances. The procedure is repeated until the cluster shapes do not change significantly.

As an additional criterion for the detection the prominence of the pattern is included. Similar shapes with steep edges in the magnetic field can also be caused by sensor noise, however these magnetic field variations are typically of low amplitude and can, therefore, be easily ignored. A shape based approach, which is invariant to scaling in the magnitude, would, however, classify instances of sensor noise as disturbances because of the similarity in shape. For this reason the relative amplitude of the pattern in respect to the typical level of variation in the sliding window is included in the recognition process. The similarity threshold used for detection is determined by minimizing the loss function

$$L = \frac{1}{N} \sum_{i}^{N} (p_i - y_i)^2 \tag{3}$$

where N is the number of samples, p_i the predicted class and y_i the predefined class for the ith samples. The computation is performed on a data set containing 1500 manually labeled samples with positive and negative examples.

In general, correction of these disturbances is difficult, as it would require a model based on the inducing currents. This is further impeded by a loss of information in the form of aliasing effects and superposition of different disturbances. However, the typical shape S obtained by clustering gives a good approximation of the average interference

in the magnetic field and is therefore suitable for an initial correction. All non-systematic features are eliminated by the computation of S, leaving only the process specific signature in the magnetic field. To realize this, the average shape S_i $i \in \{x, y, z\}$ for every of the three magnetic field components is computed as described above. Following this, the computed shapes are aligned to the identified Orbit Correction Maneuvers and scaled to actual field strength. However, these interferences are subject to slight variations caused by e.g. aliasing effects. To account for those, the matched shape S_i is adjusted so that the function

$$f_i(c) = \sum_{k=0}^{N-1} \left(B_{i,k} - A_i(c_k)\right)^2, \quad i \in \{x, y, z\} \tag{4}$$

is at its minimum. Hereby, N is the number of data points, $B_{i,k}$ is the magnetic field of component i at point k and c are coefficients of the piece-wise linear approximation of S_i of the form $A_i(c_k) = c_k + A_i(c_{k-1})$ and $A_i(c_0) = c_0$. The function f_i is minimized using the interior-point algorithm [51] with lower and upper bounds of $c_k \pm 0.5$ for every coefficient c_k. The bounds for the coefficients allow only for small modifications so that the overall shape is still maintained. Finally, the adjusted shape is subtracted from the respective magnetic field component, thereby removing the interference.

3.2. LSTM Network

In this section, details on how to efficiently train a neural network are given. In order to train a neural network a suitable set of features has to be chosen. In general the choice of features depends on the problem at hand. As the Steepened Waves are similar in shape to the solution of the inviscid Burger's Equation [52]

$$\frac{\partial B}{\partial t} + B\frac{\partial B}{\partial x} = 0 \tag{5}$$

the magnitude and its first and second derivative are chosen as features. The next step is the compilation of a training data set. Pattern recognition can be viewed as a binary classification problem with a positive and negative class. The problem is the large set of different shapes and parameters that need to be covered, especially for the negative class. By using Burger's Equation a training data set covering a large parameter space can be quickly and automatically generated. For the positive class 40000 Steepened Waves with varying skewness and width were produced. The negative class contains 40000 examples of symmetric pulses, square waves and partially obscured Steepened Waves. Finally, the design of the network was determined by means of grid search. For most applications a network with one layer is completely sufficient. The number of nodes, the activation function and other hyperparameters have to be adapted to the respective problem. To reduce overfitting, dropout was added. Training for 20 epochs takes around 8 min on a NVIDIA Tesla P100-SXM2-16GB using Tensorflow [53]. Using typical workstation GPUs (NVIDIA RTX 2070, NVIDIA GeForce 1080) computational times increase up to a factor of 5 compared to the P100. To further improve performance a feedback mechanism is used to fine tune the weights of the neural network. A subset of intervals classified by the pre-trained network is reevaluated by hand and labeled accordingly. This new data set is used to retrain the network. Its purpose is to enable the network to recognize the specific shape of Steepened Waves

encountered at the comet, whereas the pre-training focused on the general shape of Steepened Waves idealized by the Burger's Equation. Furthermore, the fine tuning has the purpose to extend the negative class by typical negative examples encountered at a comet. This second training data set consists of 1500 examples, again with a 1:1 ratio, and is, therefore, significantly smaller than the first data set used for pre-training. Fine-tuning takes up to 1 min on the P100. For the detection a sliding window approach is employed, with a minimal window size of 20 s and an overlap of 10 s. To account for the varying width of the Steepened Waves the magnetic field interval is resampled to different lengths. A Steepened Wave is correctly identified by the algorithm if a peak in probability above a certain threshold is present in the time interval of the Steepened Wave. The threshold used for identification is computed analogously to the similarity threshold in Section 3.1, using the same data set employed for fine tuning of the neural network.

For most applications in physics a simple detection of a pattern, however, is not sufficient, because for data analysis the beginning and end of a structure are important. For the application at hand neural networks are not suitable for data segmentation as they require an unreasonable amount of data to learn to distinguish suitable boundaries. Therefore, cross-correlation is used to identify the boundaries of the Steepened Waves in the window identified by the neural network, similar to Section 3.1.

4. Evaluation

4.1. Evaluation of Orbit Correction Maneuver Detection

In order to evaluate the performance of the approach presented in section 3.1 a test data set, in which all occurring Orbit Correction Maneuvers are identified by hand and labeled accordingly, is compiled. Additionally, time intervals not containing Orbit Correction Maneuvers were added to the test data set in order to evaluate the robustness of the approach in the absence of Orbit Correction Maneuvers. In total a test data set comprised of 700 Orbit Correction Maneuvers in 144 hours of magnetic field observations was used (Table 1). To evaluate the performance the metrics precision and recall [54] were employed. The precision illustrates how many positive classifications were correct and the recall how many actual positives were correctly predicted. This can be expressed as:

$$\text{precision} = \frac{\text{TP}}{\text{TP} + \text{FP}} \tag{6}$$

$$\text{recall} = \frac{\text{TP}}{\text{TP} + \text{FN}}, \tag{7}$$

hereby TP is the number of true positives, FP the number of false positives and FN the number of false negatives. The evaluation shows that above 85 % of all Orbit Correction Maneuvers present in the test data are correctly classified. The main advantage of the automatic procedure lies in the massive parallelizability and the simultaneous processing of multiple time series consisting of magnetic field observations and house keeping currents. For one day of magnetic field observations sampled at 20 Hz the average processing time amounts to approximately 10 s using 24 threads on a typical enterprise level CPU (Intel(R) Xeon(R) CPU E5-2620 using FP32), which results in a total computational time of around 2 h for 2 years of data. The top panel of Figure 3 shows the uncorrected and corrected magnetic field.

The Orbit Correction Maneuver signature visible in Figure 3(a) was removed in 3(b) with some residual fluctuations remaining. In the bottom panel the power spectral density (PSD) of the respective time intervals are depicted. Multiple peaks, which can be attributed to Orbit Correction Maneuvers, are visible in Figure 3(c). In Figure 3(d) the peaks are not visible anymore or are significantly reduced. A list of all identified Orbit Correction Maneuvers is provided as supplementary material.

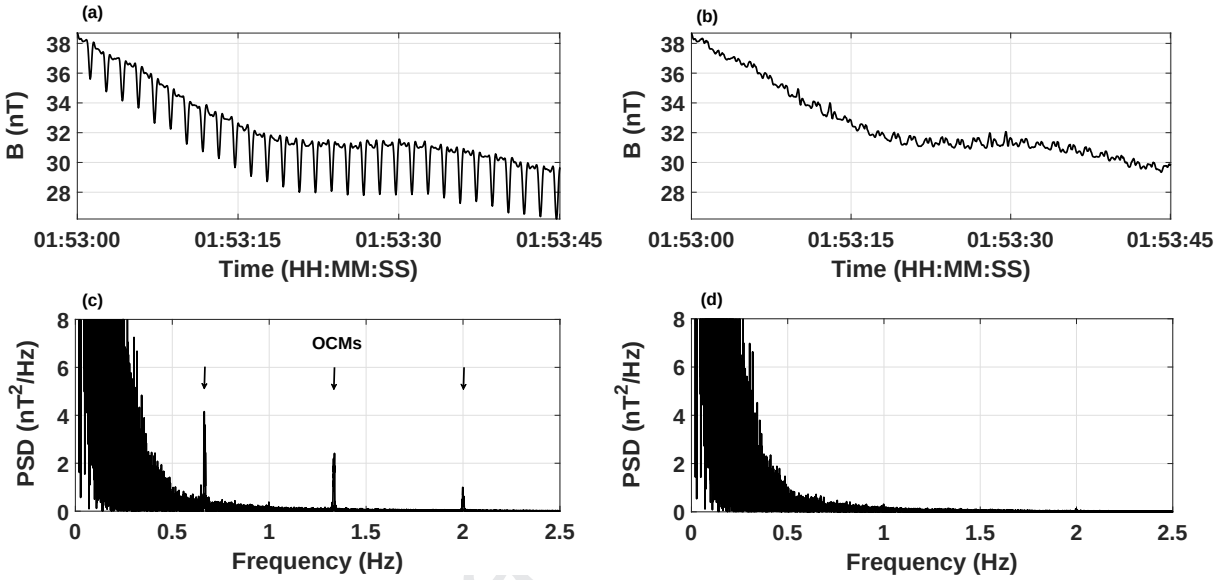

Figure 3: The top panel shows the uncorrected (left) and corrected (right) magnetic field for an exemplary time interval on August, 1st 2015. The Orbit Correction Maneuver signatures in the left figure were removed in the right figure, following the procedure described in section 3.1. The bottom panel shows the respective spectra. The spectral peaks caused by the Orbit Correction Maneuvers vanish after correction.

Orbit Correction Maneuvers	Precision	Recall
700	92.06 %	83.57 %

Table 1: Evaluation results of Orbit Correction Maneuver detection with cross-correlation.

4.2. Evaluation of Steepened Waves Detection

The performance of the procedure presented in section 3.2 is evaluated on an artificially generated and a real-world data set. The former is used to assess performance in a controlled environment and to examine limitations of the approach. On the other hand evaluation on a real-world data set illustrates the applicability in practice. The artificial test data set is generated by placing signals of varying amplitude, width and skewness, computed with Equation (5), at predefined times. To account for realistic noise and natural variations we use actual magnetic field data at where no natural Steepened Waves are present. This approach ensures a fair and comprehensible evaluation of the procedure as the times of pattern occurrences are known a priori. Evaluation was performed for a total of 96 hours of magnetic

Test Data	Steepened Waves	Precision	Recall
artificial	1250	89.01 %	85.10 %
Rosetta	460	80.62 %	82.13 %

Table 2: Precision and recall for the performance of the LSTM on the artificial and the real-world test cases.

field data with 1250 artificial Steepened Waves. The results are summarized in the top column of Table 2. For the real-life test case Steepened Waves were labeled manually for various time intervals. Figure 4 shows an example of a 22 min long magnetic field time interval, where Steepened Waves are highlighted in green and negative examples are highlighted in red. The bottom panel shows the classification probability for two different resampling factors. All true positives, false negatives and false positives are labeled accordingly in the time interval. The required time

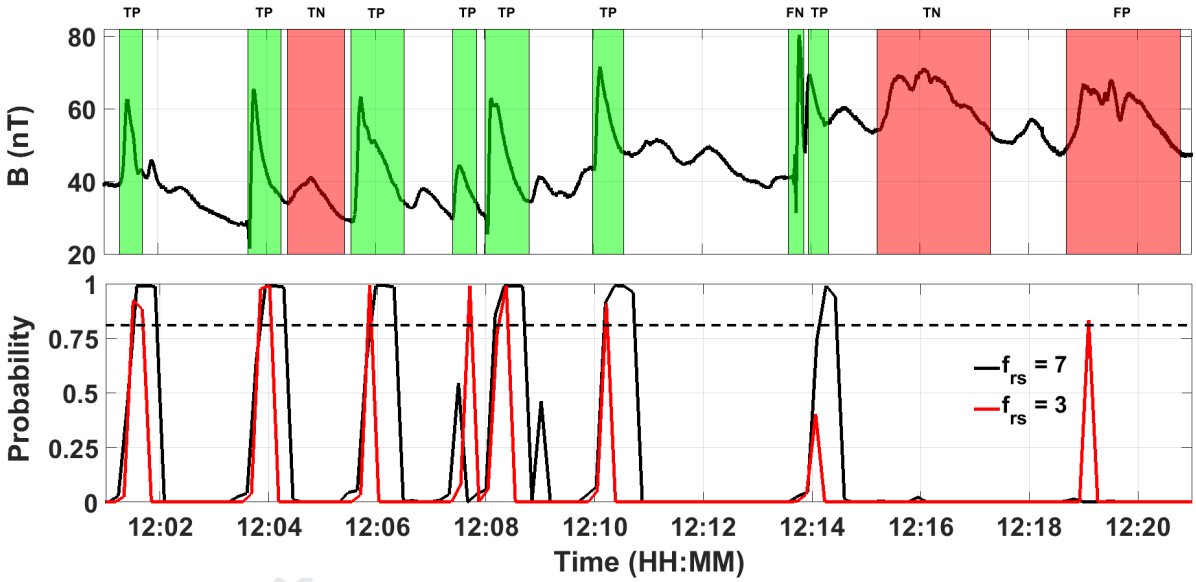

Figure 4: Example for the detection of Steepened Waves in the magnetic field for two different resampling factors. The top panel shows the magnetic field and the bottom panel depicts the probability computed by the LSTM network. The Steepened Waves labeled manually are highlighted in green. Examples for negative pattern are highlighted in red. All true positives (TP), false positives (FP) and false negatives (FN) are marked accordingly. The dashed line marks the probability threshold used for detection.

for preprocessing and pattern detection for a 24 h interval of 20 Hz amounts to around 10 seconds on a Tesla P100-SXM2, resulting in a total computational time of around 2 h for 2 years of data. However, this time span can further be reduced by splitting the data set using a divide and conquer approach. A list of all identified areas with Steepened Waves is provided as supplementary material.

5. Conclusion and Outlook

Two different methods for pattern recognition in time series were implemented and exemplarily evaluated on magnetic field data obtained during the Rosetta mission. In total a number of around 70000 Steepened Waves and 18000 Orbit Correction Maneuvers were identified in the magnetic field observations using neural networks and cross-correlation, respectively. Assuming a conservative time of 10 s per pattern required for manual selection on average, the identification per hand would have taken around 194 h for the waves and 50 h for the Orbit Correction Maneuvers, while maintaining the same coverage. The significant speed-up of up to a factor of 100 and automated fashion enable large scale statistical studies, especially for large data sets with comparatively few pattern occurrences. As background conditions for space missions cannot be controlled, contrary to laboratory studies, scientist have to rely on large data sets to enable physical interpretation. With a recall and precision above 80 % the performance is comparable to manual detection. Moreover, the automated identification is deterministic and therefore reproducible.

By computing a representative disturbance shape it was possible to correct the magnetic field so that the Orbit Correction Maneuvers signatures in the spectrum were removed. However, it has to be emphasized that the proposed method only works for recurring disturbances with a constant shape. Therefore, these time intervals still have to be evaluated with caution. For future work the mining of technical house keeping data, e.g. currents, in combination with scientific observations to detect correlated recurring patterns to identify disturbances will be the focus. This is especially useful in cases where multiply systems acting simultaneously cause a disturbance, as it is unfeasible to process such a large amount of data manually.

Another area of interest for future work is the onboard employment of pattern recognition methods. Because of power constraints, systems on board of spacecrafts are subject to strongly restricted power budgets. In this context Field Programmable Gate Arrays have gained more and more in prominence for onboard computing. Their architecture enables massive parallel processing with a relatively low power consumption. Consequently, they are a topic of interest in the context of machine learning and are perfectly suitable for onboard pattern recognition. A conservative upper bound for the power consumption for training and pattern recognition on typical Graphical Processing Units was measured to be 12 Wh for a training data set with 80000 samples and 5.2 mWh for one day of 20 Hz data respectively. With a typical power budget of at least 3 W per subsystem, onboard pattern recognition is perfectly feasible. Even onboard training is theoretically feasible if needed. This is especially applicable for the deployment of magnetometers for scientific applications as spacecrafts are subject to a magnetic cleanliness program which introduces severe limitations. In combination with a corresponding sensor configuration, pattern detection can be used to efficiently detect and correct disturbances which in turn allows to reduce magnetic cleanliness requirements.

Acknowledgements

Rosetta was an ESA mission with contributions from its member states and NASA. The contributions of the RPC-MAG team regarding the analysis and calibration of the magnetic field observations were financially supported by the

German Ministerium für Wirtschaft und Energie and the Deutsches Zentrum für Luft- und Raumfahrt under contract 50QP1401. The RPC-MAG data is available through the PSA archive of ESA and the PDS archive of NASA.

References

References

[1] H. Chen, T. Diethe, N. Twomey, P. A. Flach, Anomaly detection in star light curves using hierarchical Gaussian processes, in: 26th European Symposium on Artificial Neural Networks, ESANN, Bruges, Belgium, April 25-27, 2018. URL: http://www.elen.ucl.ac.be/Proceedings/esann/esannpdf/es2018-125.pdf.

[2] E. J. Kim, R. J. Brunner, Star-galaxy classification using deep convolutional neural networks, Monthly Notices of the Royal Astronomical Society 464 (2016) 4463–4475. doi:10.1093/mnras/stw2672.

[3] S. Navarro, R. L. M. Corradi, A. Mampaso, Automatic spectral classification of stellar spectra with low signal-to-noise ratio using artificial neural networks, Astronomy and Astrophysics 538 (2012) A76. doi:10.1051/0004-6361/201016422.

[4] C. O'Meara, L. Schlag, M. Wickler, Applications of Deep Learning Neural Networks to Satellite Telemetry Monitoring, in: 2018 SpaceOps Conference, 2018. doi:10.2514/6.2018-2558.

[5] T. Yairi, Y. Kawahara, R. Fujimaki, Y. Sato, K. Machida, Telemetry-mining: A machine learning approach to anomaly detection and fault diagnosis for space systems, in: Proceedings - SMC-IT 2006: 2nd IEEE International Conference on Space Mission Challenges for Information Technology, volume 2006, 2006, pp. 8 p – 476. doi:10.1109/SMC-IT.2006.79.

[6] E. Camporeale, S. Wing, J. R. Johnson (Eds.), Machine Learning Techniques for Space Weather, Elsevier, 2018. doi:10.1016/B978-0-12-811788-0.09989-3.

[7] S. A. Pope, T. L. Zhang, M. A. Balikhin, M. Delva, L. Hvizdos, K. Kudela, A. P. Dimmock, Exploring planetary magnetic environments using magnetically unclean spacecraft: a systems approach to VEX MAG data analysis, Annales Geophysicae 29 (2011) 639–647. doi:10.5194/angeo-29-639-2011.

[8] M. G. G. T. Taylor, N. Altobelli, B. J. Buratti, M. Choukroun, The Rosetta mission orbiter science overview: the comet phase, Philosophical Transactions of the Royal Society of London Series A 375 (2017) 20160262. doi:10.1098/rsta.2016.0262.

[9] K.-H. Glassmeier, H. Boehnhardt, D. Koschny, E. Kührt, I. Richter, The Rosetta Mission: Flying Towards the Origin of the Solar System, Space Sience Reviews 128 (2007) 1–21. doi:10.1007/s11214-006-9140-8.

[10] K.-H. Glassmeier, Interaction of the solar wind with comets: a Rosetta perspective, Philosophical Transactions of the Royal Society of London Series A 375 (2017) 20160256. doi:10.1098/rsta.2016.0256.

[11] O. Grasset, M. Dougherty, A. Coustenis, E. Bunce, C. Erd, D. Titov, M. Blanc, A. Coates, P. Drossart, L. Fletcher, H. Hussmann, R. Jaumann, N. Krupp, J.-P. Lebreton, O. Prieto-Ballesteros, P. Tortora, F. Tosi, T. V. Hoolst, JUpiter ICy moons Explorer (JUICE): An ESA mission to orbit Ganymede and to characterise the Jupiter system, Planetary and Space Science 78 (2013) 1 – 21. doi:https://doi.org/10.1016/j.pss.2012.12.002.

[12] J. Benkhoff, J. van Casteren, H. Hayakawa, M. Fujimoto, H. Laakso, M. Novara, P. Ferri, H. R. Middleton, R. Ziethe, BepiColombo-Comprehensive exploration of Mercury: Mission overview and science goals, Planetary and Space Science 58 (2010) 2 – 20. doi:10.1016/j.pss.2009.09.020.

[13] S. Besse, C. Vallat, M. Barthelemy, D. Coia, M. Costa, G. D. Marchi, D. Fraga, E. Grotheer, D. Heather, T. Lim, S. Martinez, C. Arviset, I. Barbarisi, R. Docasal, A. Macfarlane, C. Rios, J. Saiz, F. Vallejo, ESA's Planetary Science Archive: Preserve and present reliable scientific data sets, Planetary and Space Science 150 (2018) 131 – 140. Enabling Open and Interoperable Access to Planetary Science and Heliophysics Databases and Tools. doi:10.1016/j.pss.2017.07.013.

[14] P. Heinisch, H.-U. Auster, I. Richter, K.-H. Fornacon, K.-H. Glassmeier, G. Haerendel, I. Apathy, E. Cupido, Joint two-point observations of LF-waves at 67P/Churyumov—Gerasimenko, Monthly Notices of the Royal Astronomical Society 469 (2017) S68–S72. doi:10.1093/mnras/stx1175.

[15] C. Goetz, C. Koenders, D. Frühauff, I. Richter, K. H. Glassmeier, B. Tsurutani, M. Volwerk, K. C. Hansen, J. Burch, C. Carr, A. Eriksson, C. Güttler, H. Sierks, P. Henri, H. Nilsson, M. Rubin, Structure and evolution of the diamagnetic cavity at comet 67P/Churyumov–Gerasimenko, Monthly Notices of the Royal Astronomical Society 462 (2016) S459–S467. doi:10.1093/mnras/stw3148.

[16] I. Richter, H.-U. Auster, G. Berghofer, C. Carr, E. Cupido, K.-H. Fornaçon, C. Goetz, P. Heinisch, C. Koenders, B. Stoll, B. T. Tsurutani, C. Vallat, M. Volwerk, K.-H. Glassmeier, Two-point observations of low-frequency waves at 67P/Churyumov-Gerasimenko during the descent of PHILAE: comparison of RPCMAG and ROMAP, Annales Geophysicae 34 (2016) 609–622. doi:10.5194/angeo-34-609-2016.

[17] R. Hajra, J. Moré, N. Gilet, P. Henri, X. Vallières, J. L. Burch, M. Rubin, G. Wattieaux, C. Goetz, I. Richter, B. T. Tsurutani, H. Gunell, H. Nilsson, A. I. Eriksson, Z. Nemeth, Dynamic unmagnetized plasma in the diamagnetic cavity around comet 67P/Churyumov-Gerasimenko, Monthly Notices of the Royal Astronomical Society 475 (2018) 4140–4147. doi:10.1093/mnras/sty094.

[18] G. Paschmann, S. J. Schwartz, Analysis Methods For Multi-Spacecraft Data, ISSI Scientific Rep. Series SR-001, ESA/ISSI 1 (2000).

[19] K.-H. Glassmeier, U. Motschmann, R. Schmidt (Eds.), Proceedings of the Cluster Workshops, Data Analysis Tools and Physical Measurements and Mission-Oriented Theory, volume 371 of *ESA Special Publication*, 1995.

[20] A. I. Eriksson, E. Odelstad, I. A. D. Engelhardt, G. Stenberg Wieser, H. Nilsson, C. Goetz, M. Rubin, P. Henri, R. Hajra, X. Vallières, Plasma density structures at comet 67P/Churyumov–Gerasimenko, Monthly Notices of the Royal Astronomical Society 477 (2018) 1296–1307. doi:10.1093/mnras/sty765.

[21] Bieler, Andre, Altwegg, Kathrin, Balsiger, Hans, Berthelier, Jean-Jacques, Calmonte, Ursina, Combi, Michael, De Keyser, Johan, Fiethe, Björn, Fougere, Nicolas, Fuselier, Stephen, Gasc, Sébastien, Gombosi, Tamas, Hansen, Kenneth, Hässig, Myrtha, Huang, Zhenguang, Jäckel, Annette, Jia, Xianzhe, Le Roy, Lena, Mall, Urs A., Rème, Henri, Rubin, Martin, Tenishev, Valeriy, Tóth, Gábor, Tzou, Chia-Yu, Wurz, Peter, Comparison of 3D kinetic and hydrodynamic models to ROSINA-COPS measurements of the neutral coma of 67P/Churyumov-Gerasimenko, Astronomy and Astrophysics 583 (2015) A7. doi:10.1051/0004-6361/201526178.

[22] P. Lognonné, W. B. Banerdt, D. Giardini, W. T. Pike, U. Christensen, P. Laudet, S. de Raucourt, P. Zweifel, S. Calcutt, M. Bierwirth, K. J. Hurst, F. Ijpelaan, J. W. Umland, R. Llorca-Cejudo, S. A. Larson, R. F. Garcia, S. Kedar, B. Knapmeyer-Endrun, D. Mimoun, A. Mocquet, M. P. Panning, R. C. Weber, A. Sylvestre-Baron, G. Pont, N. Verdier, L. Kerjean, L. J. Facto, V. Gharakanian, J. E. Feldman, T. L. Hoffman, D. B. Klein, K. Klein, N. P. Onufer, J. Paredes-Garcia, M. P. Petkov, J. R. Willis, S. E. Smrekar, M. Drilleau, T. Gabsi, T. Nebut, O. Robert, S. Tillier, C. Moreau, M. Parise, G. Aveni, S. Ben Charef, Y. Bennour, T. Camus, P. A. Dandonneau, C. Desfoux, B. Lecomte, O. Pot, P. Revuz, D. Mance, J. tenPierick, N. E. Bowles, C. Charalambous, A. K. Delahunty, J. Hurley, R. Irshad, H. Liu, A. G. Mukherjee, I. M. Standley, A. E. Stott, J. Temple, T. Warren, M. Eberhardt, A. Kramer, W. Kühne, E.-P. Miettinen, M. Monecke, C. Aicardi, M. André, J. Baroukh, A. Borrien, A. Bouisset, P. Boutte, K. Brethomé, C. Brysbaert, T. Carlier, M. Deleuze, J. M. Desmarres, D. Dilhan, C. Doucet, D. Faye, N. Faye-Refalo, R. Gonzalez, C. Imbert, C. Larigauderie, E. Locatelli, L. Luno, J.-R. Meyer, F. Mialhe, J. M. Mouret, M. Nonon, Y. Pahn, A. Paillet, P. Pasquier, G. Perez, R. Perez, L. Perrin, B. Pouilloux, A. Rosak, I. Savin de Larclause, J. Sicre, M. Sodki, N. Toulemont, B. Vella, C. Yana, F. Alibay, O. M. Avalos, M. A. Balzer, P. Bhandari, E. Blanco, B. D. Bone, J. C. Bousman, P. Bruneau, F. J. Calef, R. J. Calvet, S. A. D'Agostino, G. de los Santos, R. G. Deen, R. W. Denise, J. Ervin, N. W. Ferraro, H. E. Gengl, F. Grinblat, D. Hernandez, M. Hetzel, M. E. Johnson, L. Khachikyan, J. Y. Lin, S. M. Madzunkov, S. L. Marshall, I. G. Mikellides, E. A. Miller, W. Raff, J. E. Singer, C. M. Sunday, J. F. Villalvazo, M. C. Wallace, D. Banfield, J. A. Rodriguez-Manfredi, C. T. Russell, A. Trebi-Ollennu, J. N. Maki, E. Beucler, M. Böse, C. Bonjour, J. L. Berenguer, S. Ceylan, J. Clinton, V. Conejero, I. Daubar, V. Dehant, P. Delage, F. Euchner, I. Estève, L. Fayon, L. Ferraioli, SEIS: Insight's Seismic Experiment for Internal Structure of Mars, Space Science Reviews 215 (2019) 12. doi:10.1007/s11214-018-0574-6.

[23] M. P. Panning, S. Kedar, Seismic response of the mars curiosity rover: Implications for future planetary seismology, Icarus 317 (2019) 373 – 378. doi:10.1016/j.icarus.2018.06.017.

[24] J. Z. D. Mieth, D. Frühauff, K.-H. Glassmeier, Statistical analysis of magnetopause crossings at lunar distances, Annales Geophysicae 37 (2019) 163–169. doi:10.5194/angeo-37-163-2019.

[25] Y.-C. Chou, L.-N. Hau, A statistical study of magnetopause structures: Tangential versus rotational discontinuities, Journal of Geophysical Research: Space Physics 117 (2012) A08232. doi:10.1029/2011JA017155.

[26] E. Liebert, C. Nabert, K.-H. Glassmeier, Statistical survey of day-side magnetospheric current flow using Cluster observations: bow shock, Annales Geophysicae 36 (2018) 1073–1080. doi:10.5194/angeo-36-1073-2018.

[27] O. Kruparova, V. Krupar, J. Šafránková, Z. Němeček, M. Maksimovic, O. Santolik, J. Soucek, F. Němec, J. Merka, Statistical Survey of the Terrestrial Bow Shock Observed by the Cluster Spacecraft, Journal of Geophysical Research: Space Physics 124 (2019) 1539–1547. doi:10.1029/2018JA026272.

[28] S. Y. Huang, J. W. Du, F. Sahraoui, Z. G. Yuan, J. S. He, J. S. Zhao, O. Le Contel, H. Breuillard, D. D. Wang, X. D. Yu, X. H. Deng, H. S. Fu, M. Zhou, C. J. Pollock, R. B. Torbert, C. T. Russell, J. L. Burch, A statistical study of kinetic-size magnetic holes in turbulent magnetosheath: MMS observations, Journal of Geophysical Research: Space Physics 122 (2017) 8577–8588. doi:10.1002/2017JA024415.

[29] G. Del Zanna, V. Andretta, The EUV spectrum of the Sun: SOHO CDS NIS irradiances from 1998 until 2010, Astronomy & Astrophysics 528 (2011) A139. doi:10.1051/0004-6361/201016106.

[30] W. J. Borucki, D. Koch, G. Basri, N. Batalha, T. Brown, D. Caldwell, J. Caldwell, J. Christensen-Dalsgaard, W. D. Cochran, E. DeVore, E. W. Dunham, A. K. Dupree, T. N. Gautier, J. C. Geary, R. Gilliland, A. Gould, S. B. Howell, J. M. Jenkins, Y. Kondo, D. W. Latham, G. W. Marcy, S. Meibom, H. Kjeldsen, J. J. Lissauer, D. G. Monet, D. Morrison, D. Sasselov, J. Tarter, A. Boss, D. Brownlee, T. Owen, D. Buzasi, D. Charbonneau, L. Doyle, J. Fortney, E. B. Ford, M. J. Holman, S. Seager, J. H. Steffen, W. F. Welsh, J. Rowe, H. Anderson, L. Buchhave, D. Ciardi, L. Walkowicz, W. Sherry, E. Horch, H. Isaacson, M. E. Everett, D. Fischer, G. Torres, J. A. Johnson, M. Endl, P. MacQueen, S. T. Bryson, J. Dotson, M. Haas, J. Kolodziejczak, J. Van Cleve, H. Chandrasekaran, J. D. Twicken, E. V. Quintana, B. D. Clarke, C. Allen, J. Li, H. Wu, P. Tenenbaum, E. Verner, F. Bruhweiler, J. Barnes, A. Prsa, Kepler Planet-Detection Mission: Introduction and First Results, Science 327 (2010) 977–980. doi:10.1126/science.1185402.

[31] S. B. Howell, C. Sobeck, M. Haas, M. Still, T. Barclay, F. Mullally, J. Troeltzsch, S. Aigrain, S. T. Bryson, D. Caldwell, W. J. Chaplin, W. D. Cochran, D. Huber, G. W. Marcy, A. Miglio, J. R. Najita, M. Smith, J. D. Twicken, J. J. Fortney, The K2 Mission: Characterization and Early Results, The Astronomical Society of the Pacific 126 (2014) 398. doi:10.1086/676406.

[32] E. A. Petigura, G. W. Marcy, A. W. Howard, A Plateau in the Planet Population below Twice the Size of Earth, The Astrophysical Journal 770 (2013) 69–90. doi:10.1088/0004-637X/770/1/69.

[33] F. Plaschke, T. Karlsson, C. Götz, C. Möstl, I. Richter, M. Volwerk, A. Eriksson, E. Behar, R. Goldstein, First observations of magnetic holes deep within the coma of a comet, Astronomy & Astrophysics 618 (2018) A114. doi:10.1051/0004-6361/201833300.

[34] K.-H. Glassmeier, I. Richter, A. Diedrich, G. Musmann, U. Auster, U. Motschmann, A. Balogh, C. Carr, E. Cupido, A. Coates, M. Rother, K. Schwingenschuh, K. Szegö, B. Tsurutani, RPC-MAG The Fluxgate Magnetometer in the ROSETTA Plasma Consortium, Space Sience Reviews 128 (2007) 649–670. doi:10.1007/s11214-006-9114-x.

[35] Glassmeier K.-H., Richter I., Koenders C., Goetz C., Eichelberger. H, Cupido E., ROSETTA RPCMAG ESCORT 1 PHASE (ESC1) CALIBRATED DATA RECORD V9.0, RO-C-RPCMAG-3-ESC1-CALIBRATED-V9.0, ESA Planetary Science Archive and NASA Planetary Data System, 2019.

[36] Glassmeier K.-H., Richter I., Koenders C., Goetz C., Eichelberger. H, Cupido E., ROSETTA RPCMAG ESCORT 2 PHASE (ESC2) CALIBRATED DATA RECORD V9.0, RO-C-RPCMAG-3-ESC2-CALIBRATED-V9.0, ESA Planetary Science Archive and NASA Planetary Data System, 2019.

[37] Glassmeier K.-H., Richter I., Koenders C., Goetz C., Eichelberger. H, Cupido E., ROSETTA RPCMAG ESCORT 3 PHASE (ESC3) CALIBRATED DATA RECORD V9.0, RO-C-RPCMAG-3-ESC3-CALIBRATED-V9.0, ESA Planetary Science Archive and NASA Planetary Data System, 2019.

[38] Glassmeier K.-H., Richter I., Koenders C., Goetz C., Eichelberger. H, Cupido E., ROSETTA RPCMAG ESCORT 4 PHASE (ESC4) CALIBRATED DATA RECORD V9.0, RO-C-RPCMAG-3-ESC4-CALIBRATED-V9.0, ESA Planetary Science Archive and NASA Planetary Data System, 2019.

[39] Glassmeier K.-H., Richter I., Koenders C., Goetz C., Eichelberger. H, Cupido E., ROSETTA RPCMAG EXTENDED MISSION PHASE 1(EXT1) CALIBRATED DATA RECORD V9.0, RO-C-RPCMAG-3-EXT1-CALIBRATED-V9.0, ESA Planetary Science Archive and NASA Planetary Data System, 2019.

[40] Glassmeier K.-H., Richter I., Koenders C., Goetz C., Eichelberger. H, Cupido E., ROSETTA RPCMAG EXTENDED MISSION PHASE 2(EXT2) CALIBRATED DATA RECORD V9.0, RO-C-RPCMAG-3-EXT1-CALIBRATED-V9.0, ESA Planetary Science Archive and NASA Planetary Data System, 2019.

[41] Glassmeier K.-H., Richter I., Koenders C., Goetz C., Eichelberger. H, Cupido E., ROSETTA RPCMAG EXTENDED MISSION PHASE 3(EXT3) CALIBRATED DATA RECORD V9.0, RO-C-RPCMAG-3-EXT1-CALIBRATED-V9.0, ESA Planetary Science Archive and NASA Planetary Data System, 2019.

[42] S. Z. Li, A. Jain (Eds.), Dynamic Time Warping (DTW), Springer US, Boston, MA, 2009, pp. 231–231. doi:10.1007/978-0-387-73003-5_768.

[43] X. Wang, A. Mueen, H. Ding, G. Trajcevski, P. Scheuermann, E. Keogh, Experimental comparison of representation methods and distance measures for time series data, Data Mining and Knowledge Discovery 26 (2013) 275–309. doi:10.1007/s10618-012-0250-5.

[44] H. Ding, G. Trajcevski, P. Scheuermann, X. Wang, E. Keogh, Querying and Mining of Time Series Data: Experimental Comparison of Representations and Distance Measures, Proc. VLDB Endow. 1 (2008) 1542–1552. doi:10.14778/1454159.1454226.

[45] L. Rabiner, B. Juang, An Introduction to Hidden Markov Models, IEEE ASSP Magazine 3 (1986) 4–16. doi:10.1109/MASSP.1986.1165342.

[46] S. Hochreiter, J. Schmidhuber, Long Short-Term Memory, Neural Comput. 9 (1997) 1735–1780. doi:10.1162/neco.1997.9.8.1735.

[47] I. Goodfellow, Y. Bengio, A. Courville, Deep Learning, The MIT Press, 2016. http://www.deeplearningbook.org.

[48] S. Butterworth, On the Theory of Filter Amplifiers, Experimental Wireless and the Wireless Engineer 7 (1930) 536–541.

[49] J. Paparrizos, L. Gravano, k-Shape: Efficient and Accurate Clustering of Time Series, SIGMOD Rec. 45 (2016) 69–76. doi:10.1145/2949741.2949758.

[50] D. Lyon, The discrete fourier transform, part 6: Cross-correlation., Journal of Object Technology 9 (2010) 17–22. doi:10.5381/jot.2010.9.2.c2.

[51] R. H. Byrd, J. C. Gilbert, J. Nocedal, A trust region method based on interior point techniques for nonlinear programming, Mathematical Programming 89 (2000) 149–185. doi:10.1007/PL00011391.

[52] J. Burgers, A Mathematical Model Illustrating the Theory of Turbulence, volume 1 of *Advances in Applied Mechanics*, Elsevier, 1948, pp. 171 – 199. doi:10.1016/S0065-2156(08)70100-5.

[53] M. Abadi, A. Agarwal, P. Barham, E. Brevdo, Z. Chen, C. Citro, G. S. Corrado, A. Davis, J. Dean, M. Devin, S. Ghemawat, I. Goodfellow, A. Harp, G. Irving, M. Isard, Y. Jia, R. Jozefowicz, L. Kaiser, M. Kudlur, J. Levenberg, D. Mané, R. Monga, S. Moore, D. Murray, C. Olah, M. Schuster, J. Shlens, B. Steiner, I. Sutskever, K. Talwar, P. Tucker, V. Vanhoucke, V. Vasudevan, F. Viégas, O. Vinyals, P. Warden, M. Wattenberg, M. Wicke, Y. Yu, X. Zheng, TensorFlow: Large-scale machine learning on heterogeneous systems, 2015. URL: https://www.tensorflow.org/, software available from tensorflow.org.

[54] D. L. Olson, D. Delen, Advanced Data Mining Techniques, 1st ed., Springer Publishing Company, Incorporated, 2008. doi:10.1007/978-3-540-76917-0.